

Hidden polar phase in the quantum paraelectric SrTiO_3 .

Huaiyu Hugo Wang^{1,2}, Ernesto Flores^{1,2}, Jade Stanton^{1,2}, Gal Orenstein^{1,2},
Peter R. Miedaner³, Laura Foglia⁴, Maya Martinez¹, David A. Reis^{1,2}, Roman Mankowsky⁵,
Mathias Sander⁵, Henrik Lemke⁵, Serhane Zerdane⁵, Keith A. Nelson³, Mariano Trigo^{1,2*}

¹Stanford Institute for Materials and Energy Sciences,

SLAC National Accelerator Laboratory, Menlo Park CA 94025, USA.

²Stanford PULSE Institute, SLAC National Accelerator Laboratory, Menlo Park, California 94025, USA

³ Department of Chemistry, Massachusetts Institute of Technology, Cambridge, Massachusetts 02138, USA

⁴ Elettra-Sincrotrone, Trieste 34149, Italy ⁵ Paul Scherrer Institut, 5232 Villigen PSI, Switzerland

*Corresponding author. Email: mtrigo@slac.stanford.edu

Hidden phases of quantum materials are collective states that exist outside the equilibrium phase diagram and can host exotic properties with transformative potential. However, because they can often mimic known states, identifying them remains challenging. Strontium titanate (SrTiO_3) epitomizes this challenge: upon cooling, it displays signatures of ferroelectricity yet never develops this order. We combined mechanical strain with ultrafast laser pulses and x-ray scattering to discover a new polar state in SrTiO_3 that is distinct from ferroelectricity. Its signature are distinctive polar vibrations with nanometer wavelengths. This reveals that strain stabilizes a hidden state characterized by a nanoscale polarization modulation rather than conventional homogeneous ferroelectricity. Our findings may offer an alternative explanation for quantum paraelectricity and demonstrate

that probing collective excitations at finite momentum is essential for identifying hidden phases in quantum materials.

Hidden phases in quantum materials have emerged as a central theme in modern condensed matter physics due to their exotic properties. These phases can be induced by ultrafast optical excitation (1–3), strain (4–6), or other non-thermal perturbations but are difficult to detect, often masquerading as other known states, mimicking their thermodynamic and macroscopic signatures. Unmasking these phases requires identifying the proper fingerprints of the hidden phase. Low-energy collective modes (7–9), relevant at low temperature, can provide such a fingerprint, but these are difficult to measure, often occurring at finite momentum, hidden from optical probes. SrTiO₃ exemplifies this challenge: upon cooling, it exhibits features of ferroelectric (FE) order, including enhanced dielectric susceptibility (10) and softening of the polar mode (11), yet it never develops long-range FE order, even at the lowest temperatures. This suppression is attributed to quantum fluctuations of ionic vibrations, making SrTiO₃ the quintessential quantum paraelectric. Despite decades of study (10, 12), the nature of its low-temperature phase remains highly debated (13, 14). Proposed explanations range from quantum critical behavior driven by ferroelectric fluctuations (12, 13) to a scenario in which ferroelectricity is preempted by a modulated polar phase arising from acoustic mode condensation at finite momentum (14–16). Here, we use uniaxial strain to stabilize a new, hidden polar phase in the quantum paraelectric SrTiO₃ and use ultrafast x-ray scattering to probe its collective polar modes (17). Under tensile strain, we observe new polar acoustic modes at finite momentum that signal a transition to a state where the polarization is modulated at nanoscale lengths. This elusive phase is distinct from the long-assumed conventional ferroelectric arising from condensation of the zone-center transverse optical phonon (18), which does not change substantially under strain in our measurements. Our results establish a new paradigm for interpreting the physics of quantum paraelectrics and underscore the broader principle that hidden phases can closely resemble known states, with their true nature potentially revealed by probing their collective excitations.

Although SrTiO₃ is traditionally characterized as a quantum paraelectric, where quantum fluctuations interrupt ferroelectric order (12), this description may overlook a more complex reality. The material exhibits quantum criticality (13, 19) and extreme sensitivity to non-thermal perturbations such as ultrafast pulses (2, 3), doping (20), oxygen substitution (21) and epitaxial strain (4, 5, 22–24),

suggesting proximity to other broken-symmetry phases (14). The true nature of this quantum paraelectric regime remains unsettled. Fig. 1A shows a schematic phase diagram (14, 19) of SrTiO₃ summarizing the competing scenarios of the low-temperature regime. Here, the tuning parameter represents various external stimuli like pressure, strain or doping. The blue region represents a ferroelectric transition in which, absent quantum fluctuations, below the Curie-Weiss temperature T_{CW} the system would spontaneously develop a homogeneous polarization. In this scenario, as the temperature decreases, the transverse optical (TO) phonon frequency at wavevector $k = 0$ decreases (softens) (18) and eventually reaches zero at T_{CW} and the mode “freezes” (blue arrow in Fig. 1 A). This drives a macroscopic lattice distortion and the associated polarization. Below the transition, a new collective mode of the broken-symmetry phase appears as shown by the dashed blue line. Importantly, the changes occur in the TO branch and are localized in the region near $k = 0$. This is the canonical picture of displacive ferroelectric phase transitions (25), although its applicability to SrTiO₃ has been questioned (13, 14, 16, 19). An alternative scenario (14, 16), is represented by the orange shaded area on the right. Here, strong interaction between the TO and the transverse acoustic (TA) modes induces softening of the TA mode at $k \neq 0$, which condenses to zero frequency at a different T_c (orange arrow in Fig. 1 A), resulting in microscopic modulation of the structure and a new amplitude mode shown by the dashed orange line. The coupling between TO and TA modes gives the TA branch a strong polar character. In contrast with the previous scenario, here the changes are primarily in the *acoustic* modes and occur at *finite* crystal-momentum. Importantly, in both cases, the susceptibility must increase near the critical temperature when the corresponding mode frequency reaches zero. This means that average macroscopic quantities may behave similarly in both phases. This underscores the need to probe the phonon modes at finite k to correctly identify the state of the system.

In this work, we applied uniaxial strain at cryogenic temperatures to tune quantum-paraelectric SrTiO₃ toward its reported ferroelectric phase (6, 22), and probed the mesoscopic polar excitations in the system using ultrafast x-ray scattering at the Bernina instrument of the SwissFEL facility (26). A single-cycle terahertz (THz) pump pulse resonantly excited the soft polar modes of SrTiO₃, followed by a femtosecond hard x-ray diffraction and diffuse scattering probe, as shown in Fig. 1B (27). In previous work, we demonstrated that this technique is uniquely sensitive to collective *polar* modes, enabling direct mapping of their energy dispersion with exceptional wavevector and energy

resolution (17). Importantly, the THz pulse does not induce a phase transformation, rather it excites the polar modes coherently in the linear response regime (17). Therefore, the collective modes observed are those near the ground state of the system. When combined with strain tuning as we show here, this approach provides access to the polarization landscape of the phase transition in strained SrTiO₃, allowing us to distinguish the polar phases presented in Fig. 1A.

Bulk single-crystal SrTiO₃ with dimensions $5 \times 0.2 \times 0.05 \text{ mm}^3$ was mounted on a tunable strain-cell and cryogenically cooled to $T = 20 \text{ K}$. Fig. 2A shows rocking curves around the (3, 3, 3) Bragg reflection (pseudo-cubic notation) taken for three strain-cell displacements ΔL . Here ΔL is the nominal change in the sample length obtained through the change in capacitance of the strain device. The strain that transfers to the sample surface illuminated by the x-rays is smaller (27). The green, red, and blue lines correspond to increasing tensile strain along the cubic [100] direction (inset of Fig. 2A). The green curve exhibits two peaks originating from distinct tetragonal domains that typically develop in unstrained SrTiO₃ below the $T = 105 \text{ K}$ antiferrodistortive phase transition (17, 28–30). As ΔL increases, the peak at 91.72° is suppressed (Fig. 2A), indicating detwinning of the sample under tensile strain towards a monodomain configuration where the tetragonal axis is expected along the tensile direction (31, 32).

With increasing tensile strain, the peak at 91.82° shifts to larger angles, reflecting the modification of the (3, 3, 3) interplanar spacing, $d_{(3,3,3)}$. Fig. 2B shows the x-ray scattering intensity as a function of the scattering angle for each strain, with the crystal orientation fixed to the maximum of the rocking curve corresponding to the same domain (the green curve was measured at 91.82°). The Bragg reflection shifts to lower scattering angles with increasing ΔL , confirming an increasing $d_{(3,3,3)}$ under tensile strain. From these shifts we obtain the changes in interplanar spacing for the red and blue curves referenced to the green curve, $\Delta d_{(3,3,3)}/\bar{d}_{(3,3,3)} = 2.60 \times 10^{-4}$ and 2.89×10^{-4} , respectively, where $\bar{d}_{(3,3,3)}$ is the nominal value at this temperature. Complementary calibration of the applied strain based on capacitance measurements of the strain device are described in (27).

Figures 3A and 3B show reciprocal-space maps of the x-ray intensity around the (3, 3, 3) Bragg reflection at $T = 300 \text{ K}$ and 20 K , respectively. The $T = 20 \text{ K}$ map (Fig. 3B) exhibits vertical streaks of strong scattering for wavevectors along the c^* direction (pseudo-cubic notation). In this notation the sample surface normal is along the pseud-cubic c^* . The associated logarithmic intensity plot along $[0, 0, l]$ is shown in Fig. 3C. Diffuse intensity is typically a signature of disorder, either

static or dynamic from lattice vibrations. Fig. 3A shows that the streak is absent at $T = 300$ K, indicating that the corresponding lattice disorder develops upon cooling. We did not observe a significant variation of the intensity in the vertical streak with increasing strain (27). This highly directional intensity distribution in momentum space reflects planar disorder in real space with planes perpendicular to c^* . The signal extends up to $l \approx 0.1$ rlu corresponding to a correlation length in real space of tens of nanometers. This lattice disorder at low temperature relaxes crystal-momentum conservation, allowing the long-wavelength THz field to excite nanometer-wavelength polar phonons (17).

To gain unique access to its polar collective modes we combine ultrafast x-ray scattering with single-cycle THz excitation. We stress that the pump pulse does not produce a structural phase transition, instead it generates coherent oscillations of the polar modes in the linear response regime (17). Fig. 3D shows the time evolution of the relative x-ray intensity following THz excitation, which appears predominantly along the vertical streak along $[0, 0, l]$ in Fig 3B. The THz pulse, measured by electro-optic sampling (27), is shown in the inset of Fig. 3C. The data in Fig. 3D were taken at the largest applied strain (blue traces in Fig. 2), with individual traces corresponding to representative wavevectors indicated in Fig. 3C; measurements at other strains are provided in the Supplementary Material (27). The oscillatory signal clearly varies significantly with wavevector. Notably, we do not observe a strong uniform polar response as the Bragg peak shows no appreciable dynamics for any of the strains measured (dark blue line in Fig. 3D).

These results identify the polar modes in SrTiO_3 and allow us to resolve their dispersion. The color maps in Figs. 4A–C represent the magnitude of the Fourier transform of the oscillatory signal at wavevectors along $[0, 0, l]$. Figs. 4A-C correspond to the three increasing strains presented in Fig. 2. At the lowest strain (Fig. 4A) we observe two dispersive modes spanning 0.3 – 1 THz and 1.2 – 2.5 THz, associated with the transverse acoustic (TA) and transverse optical (TO) phonon branches, respectively (17). With increasing tensile strain (Figs. 4B and 4C), the dispersion changes markedly as a third mode appears below the TA branch. This change is apparent in the spectra for $l = 0.08$ rlu shown in Fig. 4D, where the green, red, and blue traces correspond to the lowest, intermediate, and highest strains, respectively. Compared with the lowest strain condition (green curve), the red and blue traces exhibit an additional peak at 0.33 THz (dark orange circle). The frequency of this new peak does not change appreciably between the two strained configurations

(blue and red curves). Additionally, Fig. 4D shows that the high-frequency feature associated with the TO branch softens slightly and splits into two peaks at the highest strain, as indicated by the blue circles. This is also visible in Fig. 4C, where the TO branch exhibits a splitting that is not apparent at lower strains in Figs. 4A and B.

The marked change in the phonon dispersion shown in Fig 4A-C is a manifestation of a drastic modification of the lattice under only moderate strain. While the soft mode associated with the incipient FE order is believed to be the TO mode, the most prominent change observed here occurs in the TA branch at finite wavevectors. This is summarized schematically in Fig 4E. In the unstrained material, both TO and TA branches are doubly degenerate along $[0, 0, l]$ resulting in a total of four transverse branches in the frequency range of Figs. 4A-C. Our observations in Fig. 4 show that under moderate strain, the doubly degenerate TO branches split slightly, represented by the blue lines in Fig. 4E, while one of the initially doubly-degenerate TA branches becomes strongly renormalized, shown by the orange dashed line in Fig. 4E.

Our observation that weak uniaxial tensile strain ($\Delta L/L \sim 5 \times 10^{-3}$) produces a large, abrupt renormalization of one TA branch, reducing its frequency by nearly 50%, while only slightly splitting and softening the nearly degenerate TO modes, challenges conventional wisdom about the incipient ferroelectric state in SrTiO₃. Several external perturbations, including strain (4, 22), seemingly induce a polar phase in SrTiO₃, which is often interpreted as a ferroelectric state driven by condensation of the soft zone-center TO phonon, in analogy with other ferroelectric materials (18). This behavior is illustrated by the blue shaded region in Fig. 1A. In contrast, our results reveal only marginal changes to the TO branches under tensile strain, suggesting this scenario is unlikely. Importantly, the broken inversion symmetry in a homogeneous ferroelectric transition should modify strongly the response to THz excitation at $k = 0$, yet we observe no measurable polar response at the Bragg peak (Fig. 3D), even at the largest strain applied. This implies that inversion symmetry is not broken and the structure remains paraelectric on long length-scales.

Instead, our measurements show a pronounced renormalization of a TA branch at finite momentum with tensile strain. This behavior is a fingerprint of a strain-driven instability caused by condensation of the TA branch at finite wavevectors (14–16), as indicated in Fig. 1A by the orange region. Here, the relevant soft mode is not the TO mode at $k = 0$, but instead a TA mode at nonzero wavevector. The new “amplitude mode”, indicated by the dashed orange branch in Fig. 1A, is a

signature of this spatially inhomogeneous (*14*) phase. Because it occurs at finite wavevectors, this strain-driven instability is hidden from measurements that mainly sense the near-zero-wavevector response such as optical probes (2, 3).

The observed large change of the phonon dispersion likely modifies many of the macroscopic properties traditionally used to identify polar phase transitions in ferroelectric materials. For example, the abrupt emergence of a low-frequency polar mode leads to a sharp increase in the dielectric susceptibility, which scales with the inverse frequency of the relevant polar mode (33, 34). Additionally, second-harmonic emission is expected to be enhanced through hyper-Rayleigh scattering from the spatially modulated polar-acoustic regions (35, 36). However, these macroscopic signatures are also features of a conventional ferroelectric state, and relying on them alone can obscure the true microscopic nature of the polar phase. Our measurements uniquely access low-frequency polar collective modes in SrTiO₃ at the relevant wavevectors and show that the dominant instability under uniaxial tensile strain resides in the TA branch, giving rise to a distinct modulated polar–acoustic phase.

Our results clarify a long-standing puzzle over the nature of quantum paraelectric SrTiO₃ (*16*): ferroelectric order is impeded by a competing hidden phase that features a spatially modulated polarization resulting from a polar-acoustic instability at nanometer length-scales (*14*). Our results indicate that this hidden phase can be realized under uniaxial strain, and we identify it by the emergence of a new renormalized polar acoustic branch at finite wavevectors. Because of its low frequency, the polarization fluctuations associated with the new polar mode are enhanced in equilibrium, and this phase can therefore masquerade as a ferroelectric phase in the susceptibility. Our approach, combining THz excitation, ultrafast x-rays, and uniaxial strain, is able to identify this hidden phase by its low-energy polar collective modes. This new approach yields insights that provide a paradigm shift in the physics of quantum paraelectrics and demonstrates a new way to identify hidden phases in quantum materials.

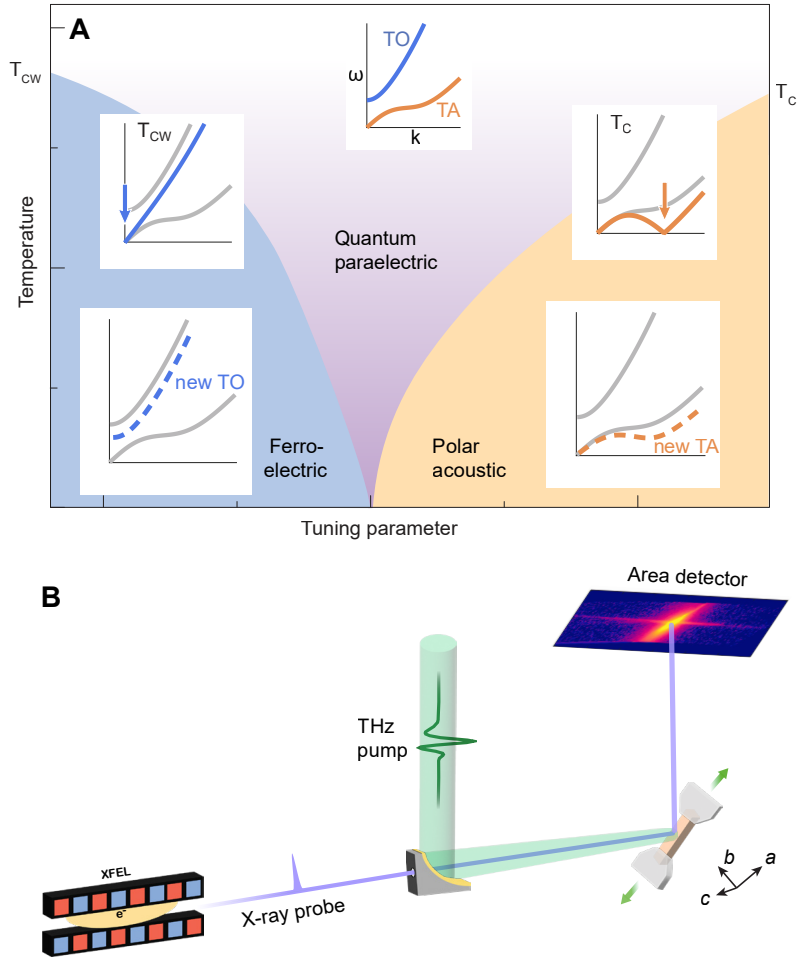


Figure 1: Ultrafast X-ray scattering from hidden quantum phases. (A) Schematic phase diagram of SrTiO₃. The ambient pressure paraelectric phase is shown in purple. The blue and orange denotes a FE phase and a polar acoustic phase (19). T_{CW} is the FE Curie-Weiss Temperature. Insets: illustrations of expected behavior of the transverse optical (TO) and acoustic (TA) phonon branches in the two phases. Blue (orange) shows the TO (TA) branch freezing at the zone center (finite wavevector) as temperature is lowered. Dashed blue and orange lines represent a new mode that appears when SrTiO₃ enters the FE and polar-acoustic phases, respectively. (B) Schematic illustration of the experimental setup at the Bernina station of the Swiss FEL. A THz pulse with a spectrum centered around 0.5 THz (Fig. S1) is focused onto a 50 μm -thick SrTiO₃ sample mounted on a Razorbill CS130 strain cell. Snapshots of the lattice are measured by diffraction of a 50 fs x-ray pulse with photon energy of 10 keV. The sample temperature was 20 K.

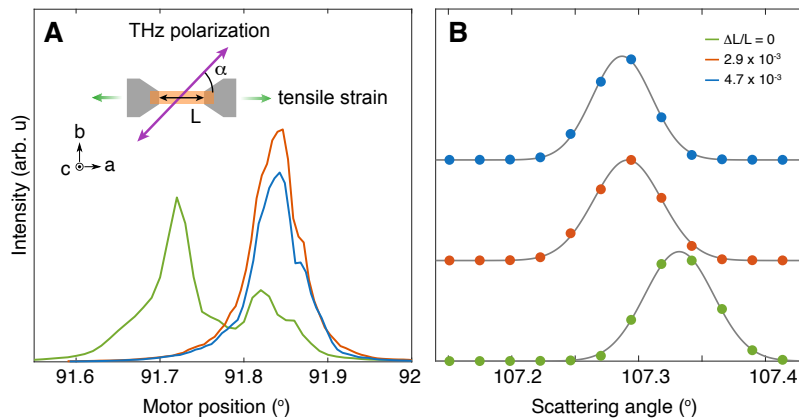


Figure 2: Structural evolution as a function of tensile strain (A) Rocking curve of the (3,3,3) Bragg peak for representative tensile strains. The change in the effective sample length from the nominal unstrained condition is labeled in the inset of B. The curves are labeled by the measured displacement of the strain-cell relative to that of the green line (27). Inset: Illustration of THz pump polarization and uniaxial strain directions with respect to crystallographic axes of the sample. **(B)** The diffraction peak profile on the detector as a function of scattering angle. The solid curves are gaussian fits.

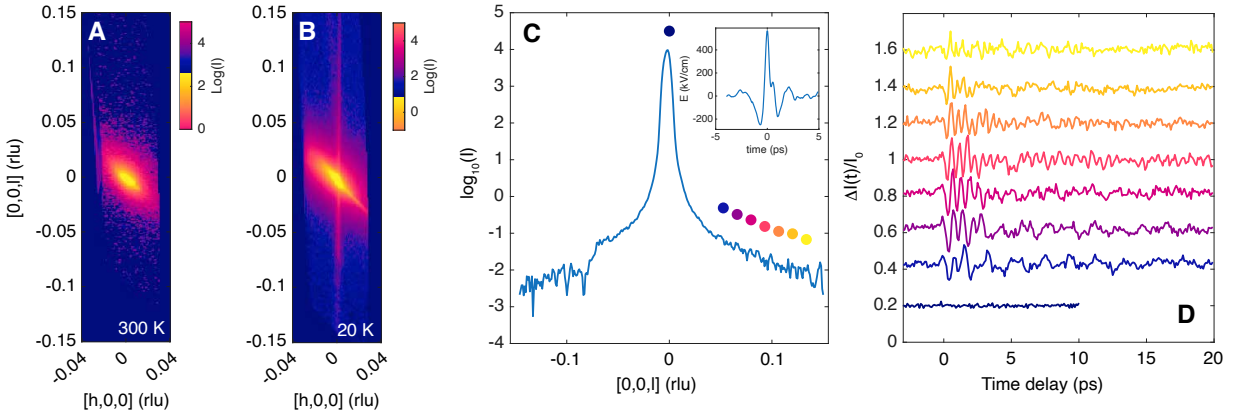


Figure 3: Coherent polar response under tensile strain. X-ray scattering intensity in reciprocal space around the (3,3,3) Bragg peak in the $[h,0,l]$ plane, at 300K (A) and 20K (B) respectively. (C) X-ray intensity along $[0,0,l]$ direction near the (3,3,3) Bragg peak (logarithmic scale). Inset: electro-optic sampling trace of THz pulse. (D) Relative x-ray intensity $\Delta I(t)/I_0$ for strain at $\Delta L/L = 4.7 \times 10^{-3}$, as a function of the delay between the THz and x-ray pulses, where $\Delta I(t) = I(t) - I_0$ and I_0 is the x-ray intensity before the THz excitation. The vertically offset lines correspond to different representative wavevectors along the $[0,0,l]$ direction indicated by the matching color dots in (C).

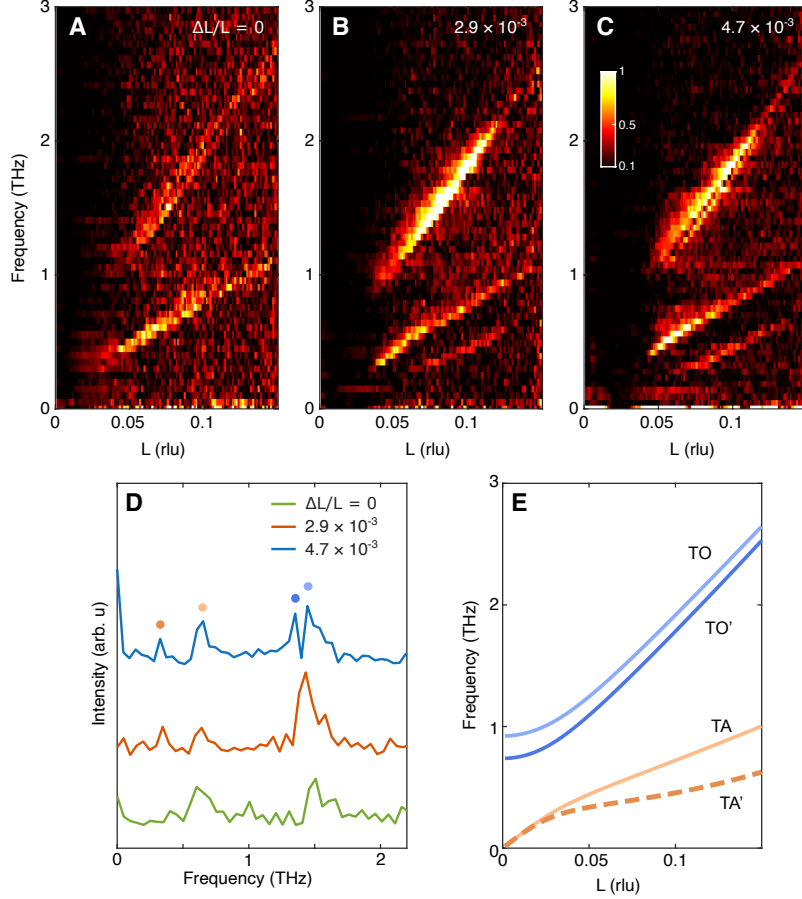


Figure 4: Collective polar modes of the hidden phase under strain. (A-C) The color maps represent the magnitude of the Fourier transform (FT) of time-domain data like those in Fig. 3D for increasing tensile strain at 20 K. (D) The magnitude of the FT at $l = 0.08$ rlu for the three strain configurations in A-C. Curves are displaced vertically for clarity. The two TA and TO phonon peaks are labeled in orange and blue dots respectively. The illustration in (E) summarizes the observed behavior under strain: two TO branches slightly frequency-split (blue curves) and a large renormalization of a one of two nearly-degenerate TA branches (dashed orange).

References and Notes

1. L. Stojchevska, *et al.*, Ultrafast Switching to a Stable Hidden Quantum State in an Electronic Crystal. *Science* **344** (6180), 177–180 (2014), doi:10.1126/science.1241591, <https://science.sciencemag.org/content/344/6180/177>.
2. X. Li, *et al.*, Terahertz field-induced ferroelectricity in quantum paraelectric SrTiO₃. *Science* **364** (6445), 1079–1082 (2019), doi:10.1126/science.aaw4913.
3. T. Nova, A. Disa, M. Fechner, A. Cavalleri, Metastable ferroelectricity in optically strained SrTiO₃. *Science* **364** (6445), 1075–1079 (2019), doi:10.1126/science.aaw4911.
4. J. H. Haeni, *et al.*, Room-temperature ferroelectricity in strained SrTiO₃. *Nature* **430** (7001), 758–761 (2004), doi:10.1038/nature02773.
5. D. G. Schlom, *et al.*, Strain Tuning of Ferroelectric Thin Films*. *Annual Review of Materials Research* **37** (Volume 37, 2007), 589–626 (2007).
6. R. Xu, *et al.*, Strain-induced room-temperature ferroelectricity in SrTiO₃ membranes. *Nature Communications* **11** (1), 3141 (2020), doi:10.1038/s41467-020-16912-3, <https://doi.org/10.1038/s41467-020-16912-3>.
7. W. Schülke, *Electron dynamics by inelastic X-ray scattering*, vol. 7 (OUP Oxford) (2007).
8. L. J. P. Ament, M. van Veenendaal, T. P. Devereaux, J. P. Hill, J. van den Brink, Resonant inelastic x-ray scattering studies of elementary excitations. *Rev. Mod. Phys.* **83**, 705–767 (2011), doi:10.1103/RevModPhys.83.705, <https://link.aps.org/doi/10.1103/RevModPhys.83.705>.
9. P. Abbamonte, J. Fink, Collective Charge Excitations Studied by Electron Energy-Loss Spectroscopy. *Annual Review of Condensed Matter Physics* **16** (Volume 16, 2025), 465–480 (2025).
10. H. Weaver, Dielectric properties of single crystals of SrTiO₃ at low temperatures. *Journal of Physics and Chemistry of Solids* **11** (3-4), 274–277 (1959), doi:10.1016/0022-3697(59)90226-4.

11. Y. Yamada, G. Shirane, Neutron Scattering and Nature of the Soft Optical Phonon in SrTiO₃. *Journal of the Physical Society of Japan* **26** (2), 396–403 (1969), doi:10.1143/JPSJ.26.396, <https://doi.org/10.1143/JPSJ.26.396>.
12. K. A. Müller, H. Burkard, SrTiO₃: An intrinsic quantum paraelectric below 4 K. *Physical Review B* **19** (7), 3593 (1979), doi:10.1103/PhysRevB.19.3593.
13. S. Rowley, *et al.*, Ferroelectric quantum criticality. *Nature Physics* **10** (5), 367–372 (2014), doi:10.1038/nphys2924.
14. G. Guzmán-Verri, C. Liang, P. Littlewood, Lamellar fluctuations melt ferroelectricity. *Physical Review Letters* **131** (4), 046801 (2023), doi:10.1103/PhysRevLett.131.046801.
15. P. Zubko, G. Catalan, A. Buckley, P. R. L. Welche, J. F. Scott, Strain-Gradient-Induced Polarization in SrTiO₃ Single Crystals. *Phys. Rev. Lett.* **99**, 167601 (2007), doi:10.1103/PhysRevLett.99.167601, <https://link.aps.org/doi/10.1103/PhysRevLett.99.167601>.
16. K. A. Müller, W. Berlinger, E. Tosatti, Indication for a novel phase in the quantum paraelectric regime of SrTiO₃. *Zeitschrift für Physik B Condensed Matter* **84**, 277–283 (1991), doi:10.1007/BF01313549.
17. G. Orenstein, *et al.*, Observation of polarization density waves in SrTiO₃. *Nature Physics* **21** (6), 961–965 (2025), doi:10.1038/s41567-025-02874-0, <https://doi.org/10.1038/s41567-025-02874-0>.
18. G. Shirane, B. C. Frazer, V. J. Minkiewicz, J. A. Leake, A. Linz, Soft Optic Modes in Barium Titanate. *Phys. Rev. Lett.* **19**, 234–235 (1967), doi:10.1103/PhysRevLett.19.234, <https://link.aps.org/doi/10.1103/PhysRevLett.19.234>.
19. M. J. Coak, *et al.*, Quantum critical phenomena in a compressible displacive ferroelectric. *Proceedings of the National Academy of Sciences* **117** (23), 12707–12712 (2020), doi:10.1073/pnas.1922151117.
20. J. G. Bednorz, K. A. Müller, Sr_{1-x}Ca_xTiO₃: An XY Quantum Ferroelectric with Transition to Randomness. *Phys. Rev. Lett.* **52**, 2289–2292 (1984), doi:10.1103/PhysRevLett.52.2289, <https://link.aps.org/doi/10.1103/PhysRevLett.52.2289>.

21. M. Itoh, *et al.*, Ferroelectricity Induced by Oxygen Isotope Exchange in Strontium Titanate Perovskite. *Physical Review Letters* **82** (17), 3540–3543 (1999), doi:10.1103/PhysRevLett.82.3540.
22. J. Li, *et al.*, The classical-to-quantum crossover in the strain-induced ferroelectric transition in SrTiO₃ membranes. *Nature Communications* **16** (1), 4445 (2025), doi:10.1038/s41467-025-59517-4, <https://doi.org/10.1038/s41467-025-59517-4>.
23. H. Uwe, T. Sakudo, Stress-induced ferroelectricity and soft phonon modes in SrTiO₃. *Phys. Rev. B* **13**, 271–286 (1976), doi:10.1103/PhysRevB.13.271, <https://link.aps.org/doi/10.1103/PhysRevB.13.271>.
24. S. Salmani-Rezaie, K. Ahadi, W. M. Strickland, S. Stemmer, Order-Disorder Ferroelectric Transition of Strained SrTiO₃. *Phys. Rev. Lett.* **125**, 087601 (2020), doi:10.1103/PhysRevLett.125.087601, <https://link.aps.org/doi/10.1103/PhysRevLett.125.087601>.
25. W. Cochran, Crystal stability and the theory of ferroelectricity. *Advances in Physics* **9** (36), 387–423 (1960), doi:10.1080/00018736000101229.
26. E. Prat, *et al.*, A compact and cost-effective hard X-ray free-electron laser driven by a high-brightness and low-energy electron beam. *Nature Photonics* **14** (12), 748–754 (2020), doi:10.1038/s41566-020-00712-8, <https://doi.org/10.1038/s41566-020-00712-8>.
27. Materials and methods are available as supplementary material.
28. F. W. Lytle, X-ray diffractometry of low-temperature phase transformations in strontium titanate. *Journal of Applied Physics* **35** (7), 2212–2215 (1964).
29. S. A. Hayward, E. K. H. Salje, Cubic-Tetragonal Phase Transition in SrTiO₃ Revisited: Landau Theory and Transition Mechanism. *Phase Transitions* **68** (3), 501–522 (1999), doi:10.1080/01411599908224530.
30. G. Shirane, Y. Yamada, Lattice-dynamical study of the 110 K phase transition in SrTiO₃. *Physical Review* **177** (2), 858 (1969), doi:10.1103/PhysRev.177.858.

31. T. S. Chang, J. F. Holzrichter, G. F. Imbusch, A. L. Schawlow, DIRECT OBSERVATION OF SINGLE-DOMAIN SrTiO₃. *Applied Physics Letters* **17** (6), 254–257 (1970), doi:10.1063/1.1653388, <https://doi.org/10.1063/1.1653388>.
32. K. Müller, W. Berlinger, M. Capizzi, H. Gränicher, Monodomain strontium titanate. *Solid State Communications* **8** (7), 549–553 (1970), doi:[https://doi.org/10.1016/0038-1098\(70\)90302-9](https://doi.org/10.1016/0038-1098(70)90302-9), <https://www.sciencedirect.com/science/article/pii/0038109870903029>.
33. R. H. Lyddane, R. G. Sachs, E. Teller, On the Polar Vibrations of Alkali Halides. *Phys. Rev.* **59**, 673–676 (1941), doi:10.1103/PhysRev.59.673, <https://link.aps.org/doi/10.1103/PhysRev.59.673>.
34. J. F. Scott, Soft-mode spectroscopy: Experimental studies of structural phase transitions. *Rev. Mod. Phys.* **46**, 83–128 (1974), doi:10.1103/RevModPhys.46.83, <https://link.aps.org/doi/10.1103/RevModPhys.46.83>.
35. K. Inoue, Study of structural phase transitions by the hyper-Raman scattering. *Ferroelectrics* **52** (1), 253–262 (1983).
36. A. Al-Zein, J. Hlinka, J. Rouquette, A. Kania, B. Hehlen, Hyper-Raman scattering: New prospects for the description of the local structure of complex perovskites. *Journal of Applied Physics* **109** (12), 124114 (2011), doi:10.1063/1.3599863, <https://doi.org/10.1063/1.3599863>.
37. R. Mankowsky, *et al.*, New insights into correlated materials in the time domain—combining far-infrared excitation with x-ray probes at cryogenic temperatures. *Journal of Physics: Condensed Matter* **33** (37), 374001 (2021).
38. H. Hirori, F. Blanchard, K. Tanaka, *et al.*, Single-cycle terahertz pulses with amplitudes exceeding 1 MV/cm generated by optical rectification in LiNbO₃. *Applied Physics Letters* **98** (9) (2011).

Acknowledgments

We acknowledge the Paul Scherrer Institute, Villigen, Switzerland for provision of free-electron laser beamtime at the Bernina instrument of the SwissFEL ARAMIS branch.

Funding: H.W., J.S., D.A.R. and M.T. were supported by the US Department of Energy, Office of Science, Office of Basic Energy Sciences through the Division of Materials Sciences and Engineering under Contract No. DE-AC02-76SF00515. E.F. was supported by N.S.F. fellowship DGE-2146755. P.M. was supported by an XtalPi AI for Science fellowship. G.O. acknowledges support from the Koret Foundation.

Author contributions: M.T. conceived and supervised the project. H.W. led the experiment. H.W., J.S., E.F., G.O., P.M., L.F., R.M., M.S., H.L., S.Z., M.T. performed the experiment. M.M. and H.W. prepared the samples. H.W., G.O. and M.T. wrote the initial manuscript with feedback from all authors.

Competing interests: There are no competing interests to declare.

Data and materials availability: The data supporting the findings of this study are reported in the main text and supplementary materials. Raw data are available from the corresponding author upon reasonable request.

Supplementary materials

Materials and Methods

Figs. S1 to S3

Supplementary Materials for

Hidden polar phase in the quantum paraelectric SrTiO₃.

Huaiyu (Hugo) Wang^{1,2}, Ernesto Flores^{1,2}, Jade Stanton^{1,2}, Gal Orenstein^{1,2}, Peter R. Miedaner³,
Laura Foglia⁴, Maya Martinez¹, David A. Reis^{1,2}, Roman Mankowsky⁵, Mathias Sander⁵,
Henrik Lemke⁵, Serhane Zerdane⁵, Keith A. Nelson³, Mariano Trigo^{1,2*}

¹Stanford Institute for Materials and Energy Sciences, SLAC National Accelerator Laboratory, Menlo Park
CA 94025, USA.

²Stanford PULSE Institute, SLAC National Accelerator Laboratory, Menlo Park, California 94025, USA

³ Department of Chemistry, Massachusetts Institute of Technology, Cambridge, Massachusetts 02138, USA

⁴ Elettra-Sincrotrone, Trieste 34149, Italy

⁵ Paul Scherrer Institut, Villigen, Switzerland

*Corresponding author. Email: mtrigo@slac.stanford.edu

This PDF file includes:

Materials and Methods

Figures S1 to S3

Materials and Methods

A single crystal of (001)-oriented SrTiO₃ (MTI Corp) was polished and cut to $5 \times 0.2 \times 0.05$ mm³. The strain was controlled using a CS130 cell from Razorbill. The needle-shaped single crystal was suspended freely between two mounting plates of the strain cell and glued using a two-part epoxy, such as 5-minute epoxy gel and 2-ton epoxy gel from Devcon. The capacitance between the two plates provides an estimate of applied displacement.

Hard X-ray pulses with a 40 fs duration and 10.2 keV photon energy from the SwissFEL facility were monochromatized by a double crystal Silicon monochromator and focused using Kirkpatrick–Baez mirrors to a 100×100 μm² cross section at the sample. The X-ray pulses passed through a hole in a parabolic mirror used to focus the THz pulses as shown in Fig. 1B. The strain cell with the sample was mounted inside a cryogenic vacuum chamber (37) with translation and rotation motions required for diffraction. The temperature was measured by a diode fixed close to the strain cell. Intense THz fields were generated by the pulse-front-tilt method in a LiNbO₃ prism (38). The THz pulses were vertically polarized with a maximum peak electric field of around 600 kV cm⁻¹, as calibrated by electro-optic sampling measurements (Fig. 3C inset) using a 100 μm-thick GaP crystal mounted next to the sample. The Fourier spectrum of the THz pulse is shown in Fig. S1. The THz beam was focused to an 800×800 μm² beam size on the sample collinearly with the X-ray beam using a parabolic mirror.

X-ray diffraction patterns around (3, 3, 3) diffraction peak were acquired as a function of the delay between THz pump and X-ray probe pulses. The scattered photons were recorded by a Jungfrau area detector positioned at 180 mm from the sample outside of the cryogenic chamber. To match the pumped and probed volumes while maximizing the pump fluence, we implemented a grazing exit geometry. The exit angle was set to about 1° with respect to the sample surface such that the detected X-ray photons originated from a depth of < 1 μm from the sample surface, comparable to the penetration depth of the THz pulse in SrTiO₃ at low temperatures. The shot-by-shot detector images were grouped into laser-on and laser-off data sets and binned into 50 fs time bins. Typically, around 1300 events were accumulated for each data point.

The Razorbill CS130 strain cell uses parallel plate capacitive sensors to measure the displacement of the sample. The capacitance-displacement relation was calibrated at room temperature,

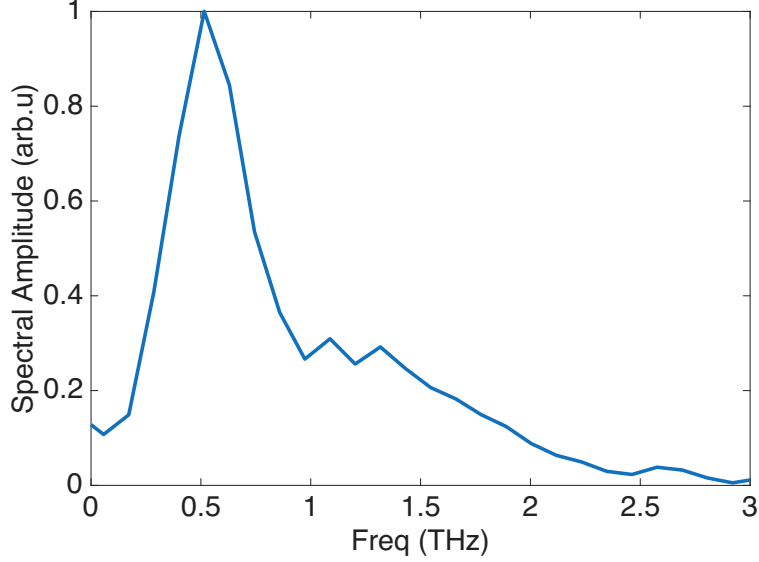


Figure S1: THz pump field spectrum. Fourier transform of the electro-optic sampling trace shown in the inset of Fig. 3C.

and the capacitance at zero tension was calibrated as a function of temperature. The effective length L is defined as the distance between two extremes of the sample glued to the cell plates. The displacement ΔL is obtained from the capacitance readings. The relative displacement $\Delta L/L$ is used to illustrate the strain condition in the main figures.

The reading of relative displacement based on the capacitance $\Delta L/L$ may differ from the actual strain transferred to the region of the sample illuminated by the x-rays. To estimate the strain on the illuminated spot of the sample we use the measured scattering angle (“two-theta”) and Bragg’s law to obtain the average change in the (3, 3, 3) lattice plane spacing. In the main text we report the relative changes, $\Delta d_{(3,3,3)}/\bar{d}_{(3,3,3)}$, where $\bar{d}_{(3,3,3)}$ is the nominal (3, 3, 3) lattice plane spacing of the unstrained sample. The results do not depend on the exact value of $\bar{d}_{(3,3,3)}$.

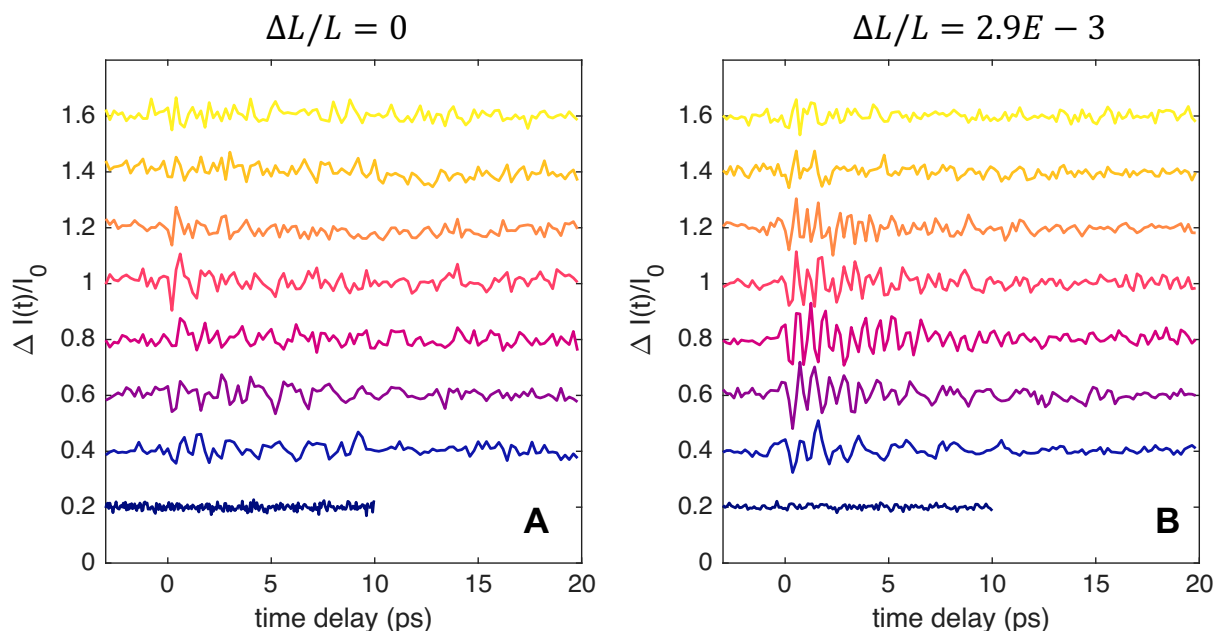


Figure S2: Relative diffraction intensity changes as a function of wave vector, delay time and strain. Relative change in diffraction intensity ($\Delta I(t)/I_0$) for representative wavevectors along the $[0,0, l]$ direction indicated by the color-coded dots in Fig. 3C at (A) $\Delta L/L = 0$ and (B) $\Delta L/L = 2.9 \times 10^{-3}$ strain conditions.

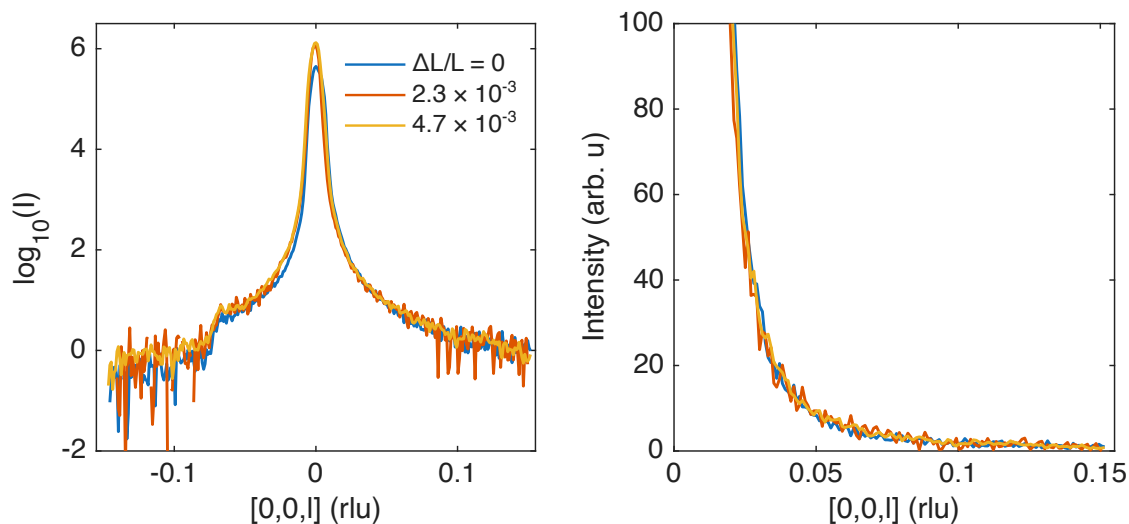


Figure S3: Intensity along (00L) for the three strain conditions. A-B show the intensity of the (00L) cut of reciprocal space for several strain configurations labeled by $\Delta L/L$. A and B show the logarithmic (base 10) and linear scale, respectively.